Supplementary Materials for

Realizing excellent conversion efficiency of 14.5% in Mg_3Sb_2/GeTe-based thermoelectric module for waste heat recovery

Xiaofang Li[a]†, Chen Chen[b]†*, Li Yin[c]†, Xinyu Wang[d], Jun Mao[c, e], Feng Cao[a]*, and Qian Zhang[c, e]*

[a]*School of Science*, *Harbin Institute of Technology*, *Shenzhen 518055*, *China*

[b]*School of Physical Sciences*, *Great Bay University*, *Dongguan 523000*, *China*

[c]*School of Materials Science and Engineering*, *and Institute of Materials Genome & Big Data*, *Harbin Institute of Technology*, *Shenzhen 518055*, *China*

[d]*Institute for Advanced Materials, Hubei Normal University, Huangshi 435002, China*

[e]*State Key Laboratory of Advanced Welding and Joining*, *Harbin Institute of Technology*, *Harbin 150001*, *China*

†These authors contributed equally to this work.

*Corresponding author. Email: ccmldn@gbu.edu.cn; caofeng@hit.edu.cn; zhangqf@hit.edu.cn.

This supplement file includes

Supplementary Tables 1-3
Supplementary Figures 1-15

Table S1 Actual chemical compositions of $Mg_{3.2}Sb_{1.99-x}Bi_xSe_{0.01}$ (x = 0.5, 0.75, 1, 1.25, and 1.5) and $Mg_{3.15}Co_{0.05}Sb_{1.24}Bi_{0.75}Se_{0.01}$ determined by EDS.

Nominal composition	Actual composition
$Mg_{3.2}Sb_{1.49}Bi_{0.5}Se_{0.01}$	$Mg_{3.015}Sb_{1.490}Bi_{0.489}Se_{0.008}$
$Mg_{3.2}Sb_{1.24}Bi_{0.75}Se_{0.01}$	$Mg_{3.017}Sb_{1.240}Bi_{0.733}Se_{0.008}$
$Mg_{3.2}Sb_{0.99}BiSe_{0.01}$	$Mg_{3.027}Sb_{0.990}Bi_{0.985}Se_{0.009}$
$Mg_{3.2}Sb_{0.74}Bi_{1.25}Se_{0.01}$	$Mg_{3.013}Sb_{0.740}Bi_{1.234}Se_{0.009}$
$Mg_{3.2}Sb_{0.49}Bi_{1.5}Se_{0.01}$	$Mg_{3.014}Sb_{0.490}Bi_{1.482}Se_{0.008}$
$Mg_{3.15}Co_{0.05}Sb_{1.24}Bi_{0.75}Se_{0.01}$	$Mg_{2.982}Co_{0.029}Sb_{1.240}Bi_{0.732}Se_{0.007}$

Table S2 Room temperature electrical properties (including electrical conductivity, Seebeck coefficient, Hall carrier concentration, Hall carrier mobility, and band gap) of $Mg_{3.2}Sb_{1.99-x}Bi_xSe_{0.01}$ (x = 0.5, 0.75, 1, 1.25, and 1.5).

Content	σ (10^4 S m^{-1})	S (μV K^{-1})	$\|n\|_H$ (10^{19} cm^{-3})	μ_H (cm^2 V^{-1} s^{-1})	E_g* (eV)
x = 0.5	2.79	-235.2	2.0	83.6	0.43
x = 0.75	3.31	-230.9	2.2	100.8	0.39
x = 1	4.41	-207.0	2.4	116.8	0.36
x = 1.25	6.04	-196.8	2.6	143.5	0.29
x = 1.5	6.58	-190.4	2.7	155.7	0.23

*The band gap was estimated by Goldsmid-Sharp formula: $E_g = 2e|S_{max}|T_{max}$.[1]

Table S3 Finite element simulation setting parameters.

Parameter	Value
Total cross-sectional area A_{pn}	2×3.6×3.6 mm^2
Cold-side thermal contact resistance	1.2×10^4 W m^{-2} K^{-1}
Hot-side thermal contact resistance	2×10^3 W m^{-2} K^{-1}
Electrical contact resistivity	20 μΩ·cm^2
Cold-side temperature	293 K
Hot-side temperature	773 K

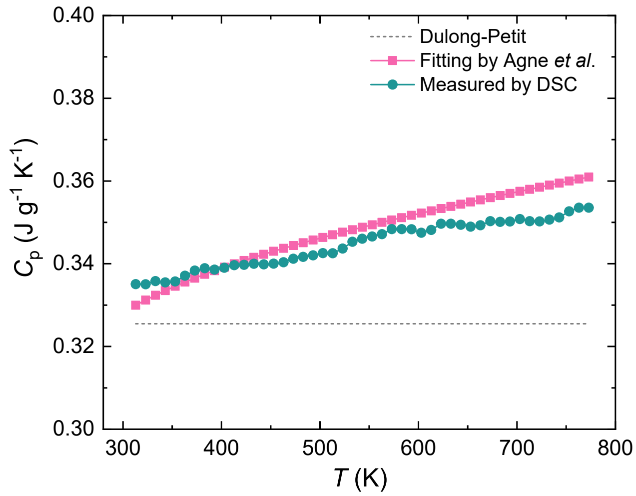

Fig. S1 Temperature-dependent heat capacity (C_p) of $Mg_{3.15}Co_{0.05}Sb_{1.24}Bi_{0.75}Se_{0.01}$. The fitting curve is obtained using the equation proposed by Agne *et al.*,[2] in comparison to the Dulong-Petit law and DSC measurement.

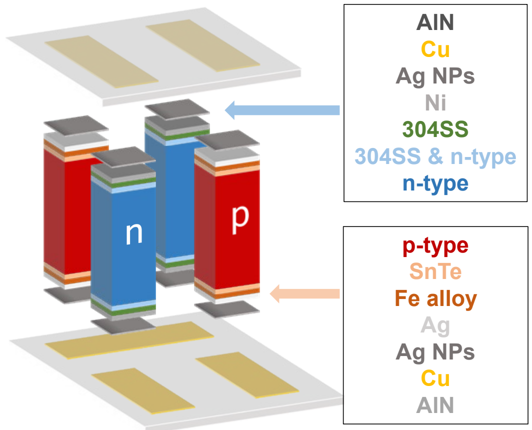

Fig. S2 Schematic of module structure design. The n-type part includes thermoelectric legs, transition layers (304SS mixed with n-type TE materials, with a mass ratio of 1:1), barrier layers (304SS), metalization layer (Ni), solder layers (Ag NPs), electrode layers (Cu), and pre-circuited AlN ceramic plates. The p-type part includes thermoelectric legs, transition layers (SnTe), barrier layers (Fe alloy), metalization layer (Ag), solder layers (Ag NPs), electrode layers (Cu), and pre-circuited AlN ceramic plates.

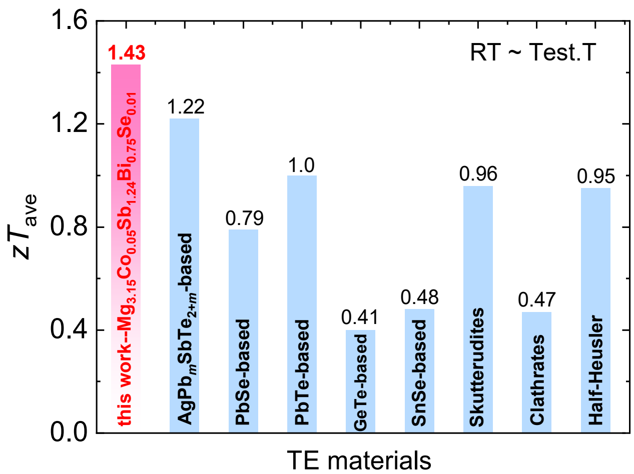

Fig. S3 Comparison of the average *zT* from room temperature to test temperature between the optimized sample ($Mg_{3.15}Co_{0.05}Sb_{1.24}Bi_{0.75}Se_{0.01}$) in this work and other typical advanced n-type TE materials.

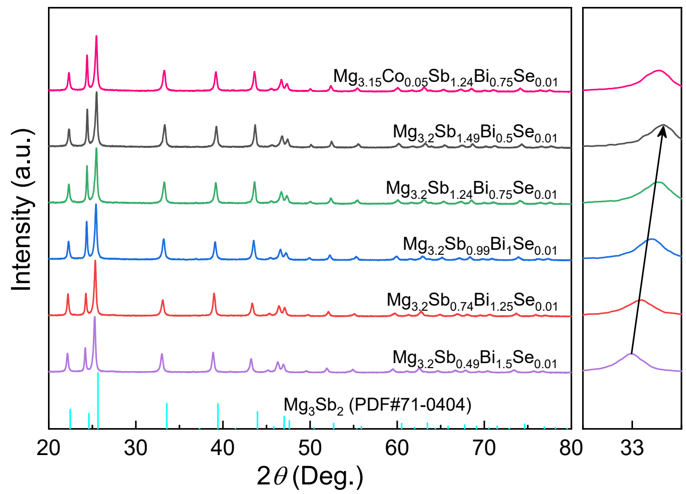

Fig. S4 XRD patterns of $Mg_{3.2}Sb_{1.99\text{-}x}Bi_xSe_{0.01}$ (x = 0.5, 0.75, 1, 1.25, and 1.5).and $Mg_{3.15}Co_{0.05}Sb_{1.24}Bi_{0.75}Se_{0.01}$. All the diffraction peaks can be indexed by the trigonal α-Mg_3Sb_2 phase (PDF#71-0404) with a $P\bar{3}m1$ space group, and the peak positions shift to a larger angle with the decrease of Bi content.

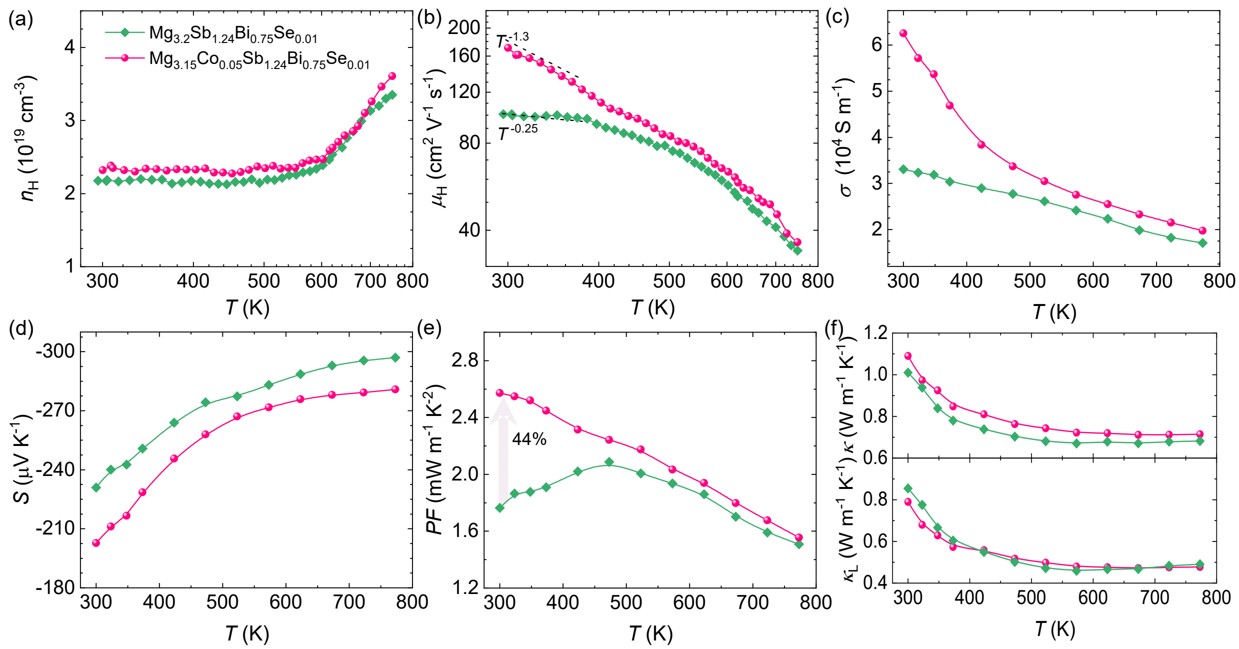

Fig. S5 Temperature-dependent (a) Hall carrier concentration, (b) Hall carrier mobility, (c) electrical conductivity, (d) Seebeck coefficient, (e) power factor, (f) total thermal conductivity and lattice thermal conductivity of $Mg_{3.2}Sb_{1.24}Bi_{0.75}Se_{0.01}$ and $Mg_{3.15}Co_{0.05}Sb_{1.24}Bi_{0.75}Se_{0.01}$.

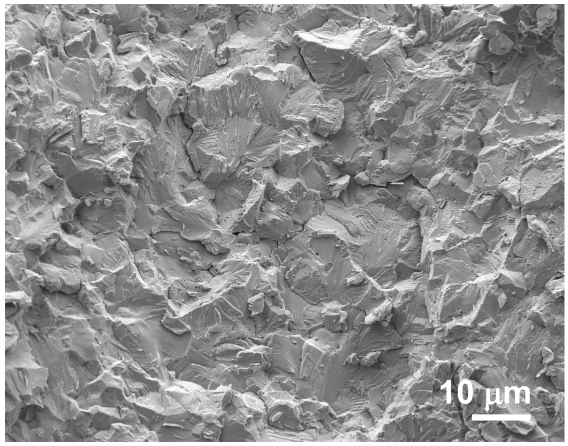

Fig. S6 The SEM images of the fracture morphology of the $Mg_{3.15}Co_{0.05}Sb_{1.24}Bi_{0.75}Se_{0.01}$ sample.

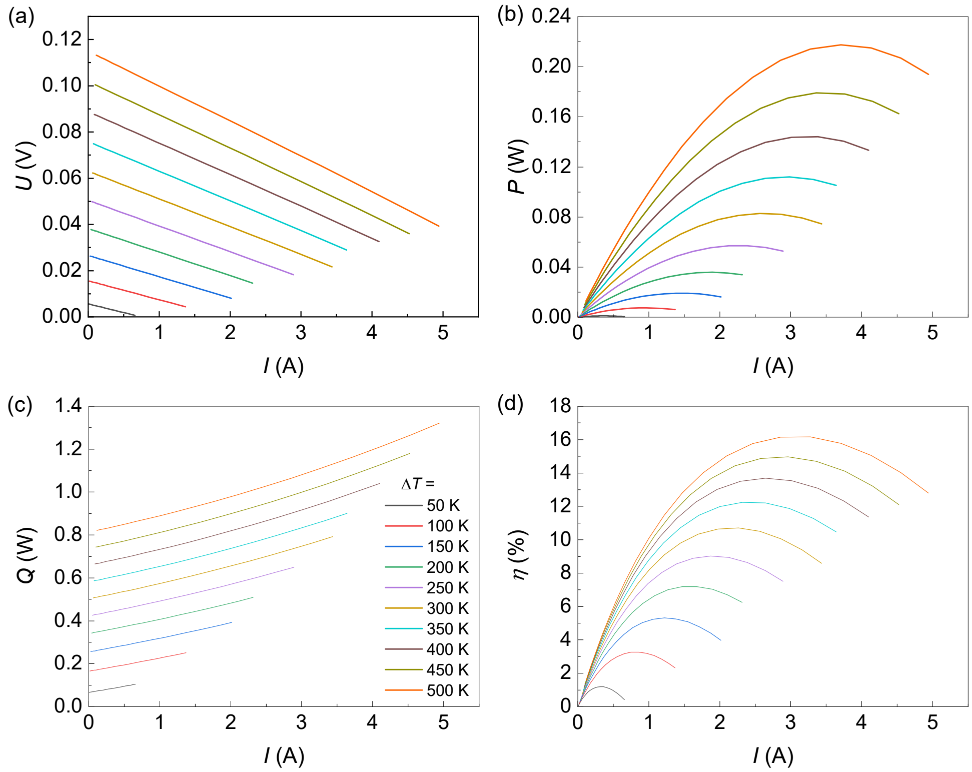

Fig. S7 Simulated properties of the n-type single-leg device ($Mg_{3.15}Co_{0.05}Sb_{1.24}Bi_{0.75}Se_{0.01}$). Current-dependent (a) output voltage, (b) output power, (c) heat flow, and (d) efficiency for the single-leg device at different temperature differences.

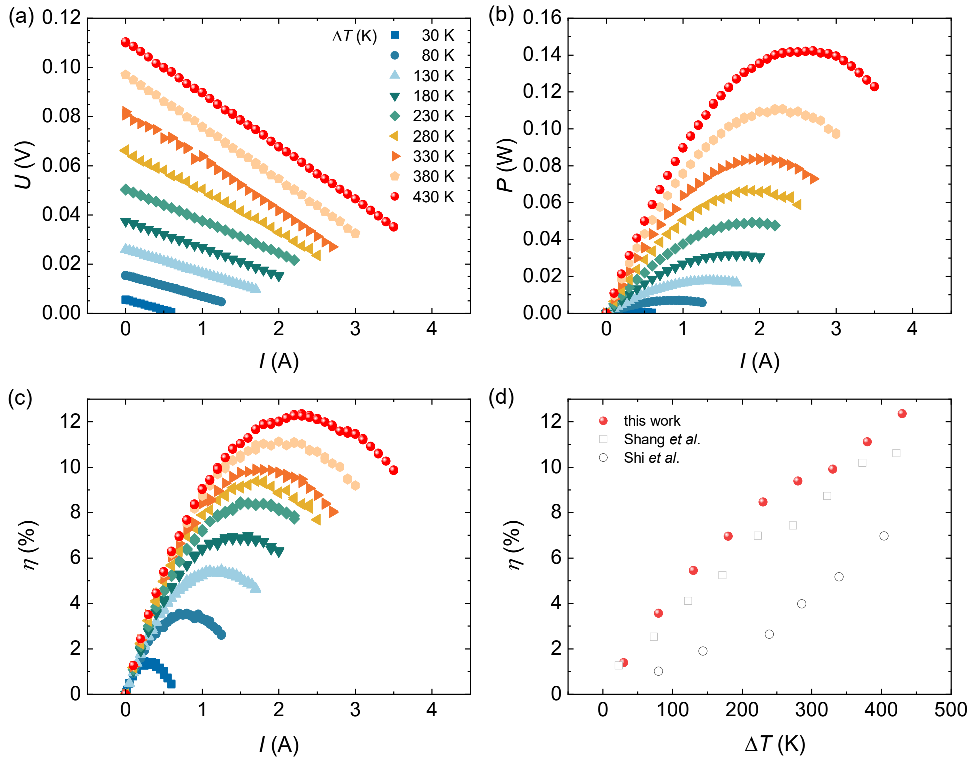

Fig. S8 Measured properties of n-type single-leg device ($Mg_{3.15}Co_{0.05}Sb_{1.24}Bi_{0.75}Se_{0.01}$). Current-dependent (a) output voltage, (b) output power, and (c) efficiency for the single-leg device at different temperature difference. (d) Comparison of the maximum efficiency in this work and literature results at different temperature difference.

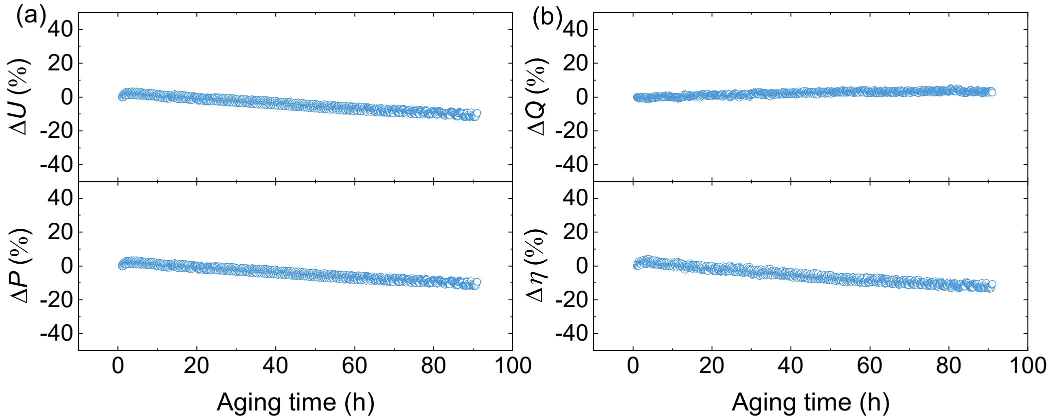

Fig. S9 Thermal aging test results (90-hour aging at T_h = 723 K and a ΔT of 430 K.) for n-type single-leg device ($Mg_{3.15}Co_{0.05}Sb_{1.24}Bi_{0.75}Se_{0.01}$). Showing changes in (a) output voltage and output power, (b) heat flow at maximum efficiency and maximum efficiency as a function of thermal cycle number.

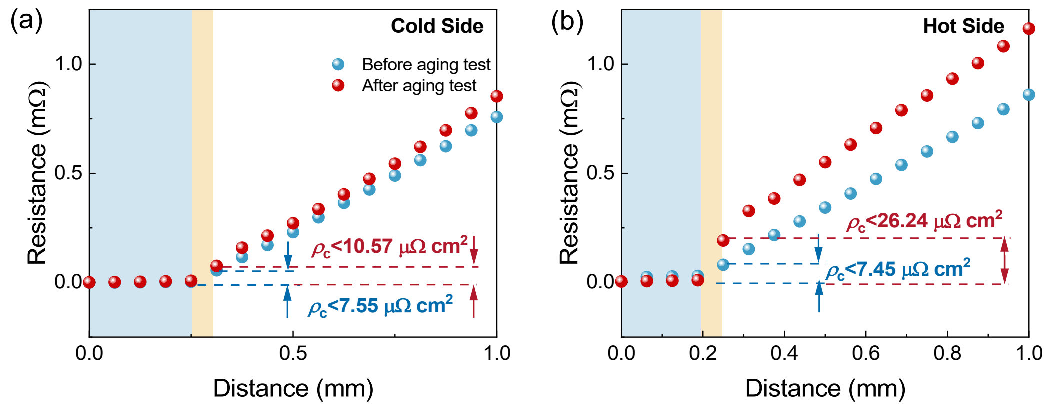

Fig. S10 Resistance scanning results for n-type (left-304SS/right- $Mg_{3.15}Co_{0.05}Sb_{1.24}Bi_{0.75}Se_{0.01}$) junctions, before and after aging test (90-hour aging at T_h = 723 K and a ΔT of 430 K.). (a) at cold side; (b) at hot side.

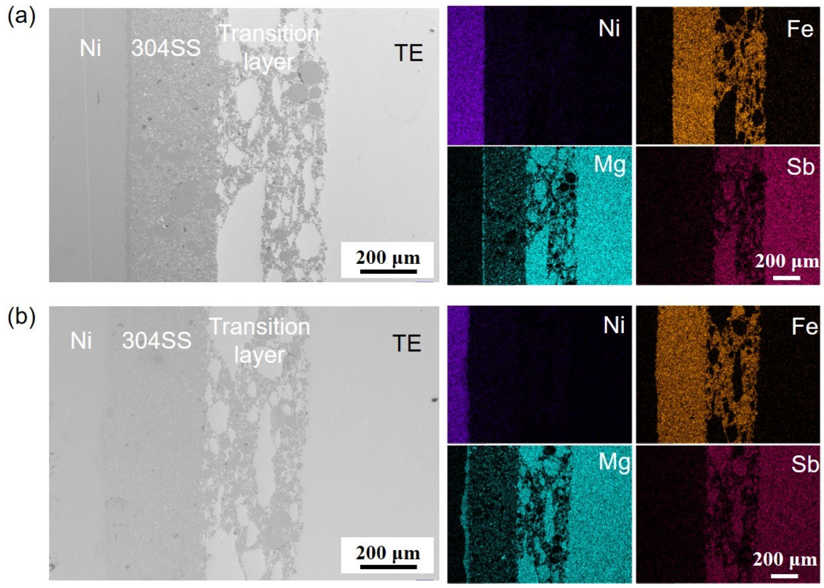

Fig. S11 SEM images and EDS mapping results of the hot side 304SS/$Mg_{3.15}Co_{0.05}Sb_{1.24}Bi_{0.75}Se_{0.01}$ junctions (a) as-prepared, and (b) aging at T_h = 723 K and a ΔT of 430 K for 90 hours. The transition layer is a mixture of n-type TE materials with 304SS, with a mass ratio of 1:1.

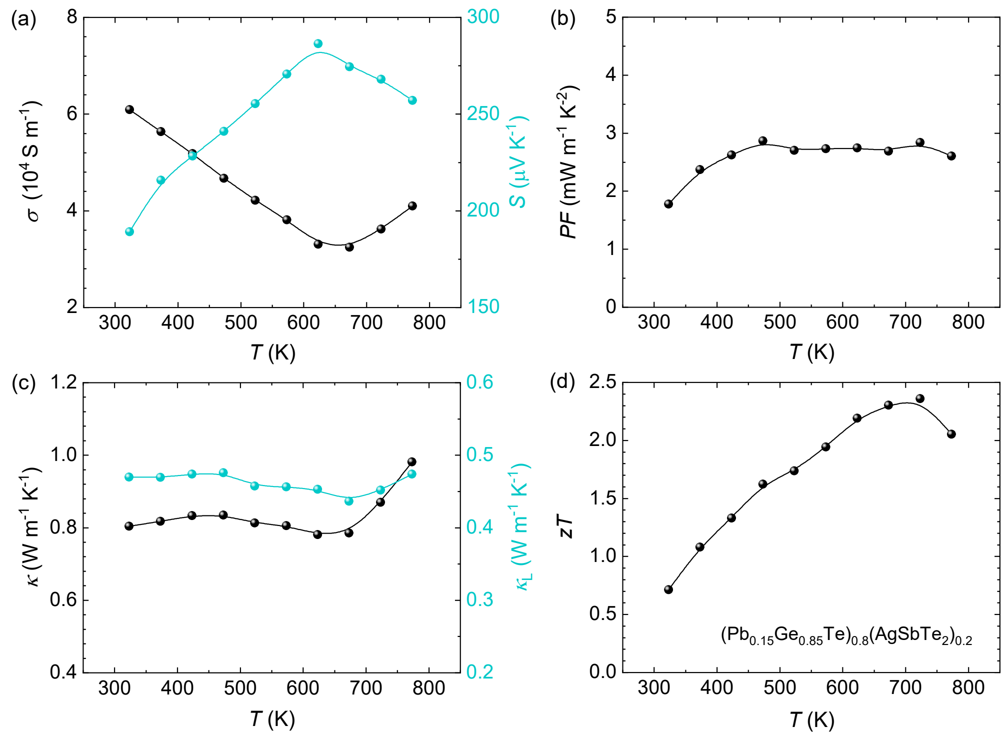

Fig. S12 Temperature-dependent (a) electrical conductivity and Seebeck coefficient, (b) power factor, (c) total thermal conductivity and lattice thermal conductivity, and (d) *zT* values of $(Pb_{0.15}Ge_{0.85}Te)_{0.8}(AgSbTe_2)_{0.2}$.

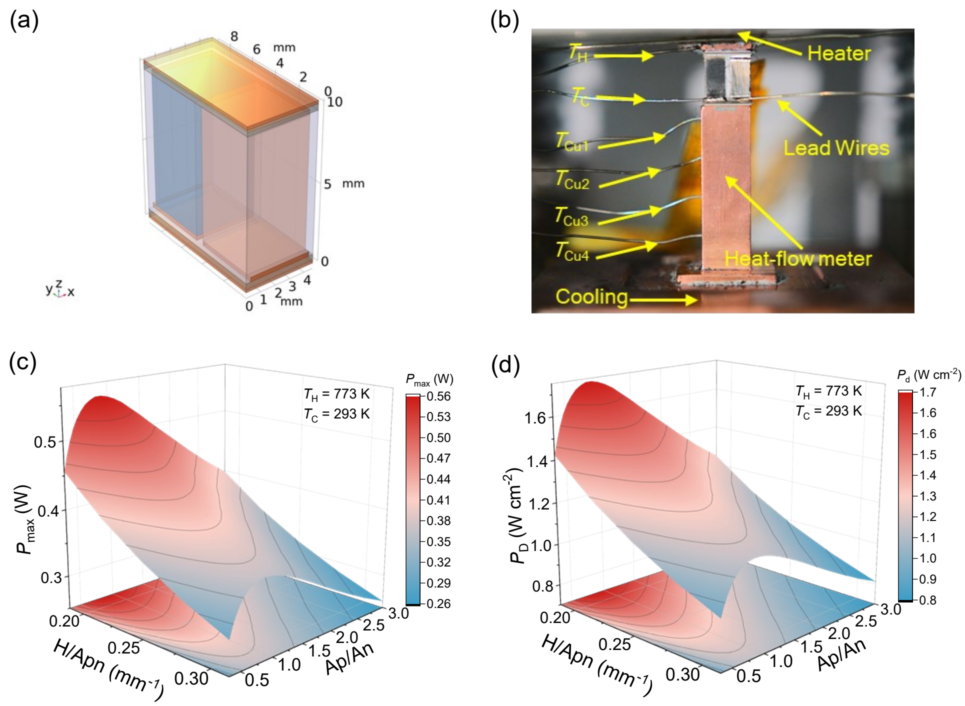

Fig. S13 3D plots of (a) unit couple, (c) the maximum output power (*P*), and (d) the maximum power density (P_D) based on calculation results for the boundary conditions specified by T_h = 773 K and T_c = 293 K. (b) Schematic diagram of the energy conversion efficiency measurement system.

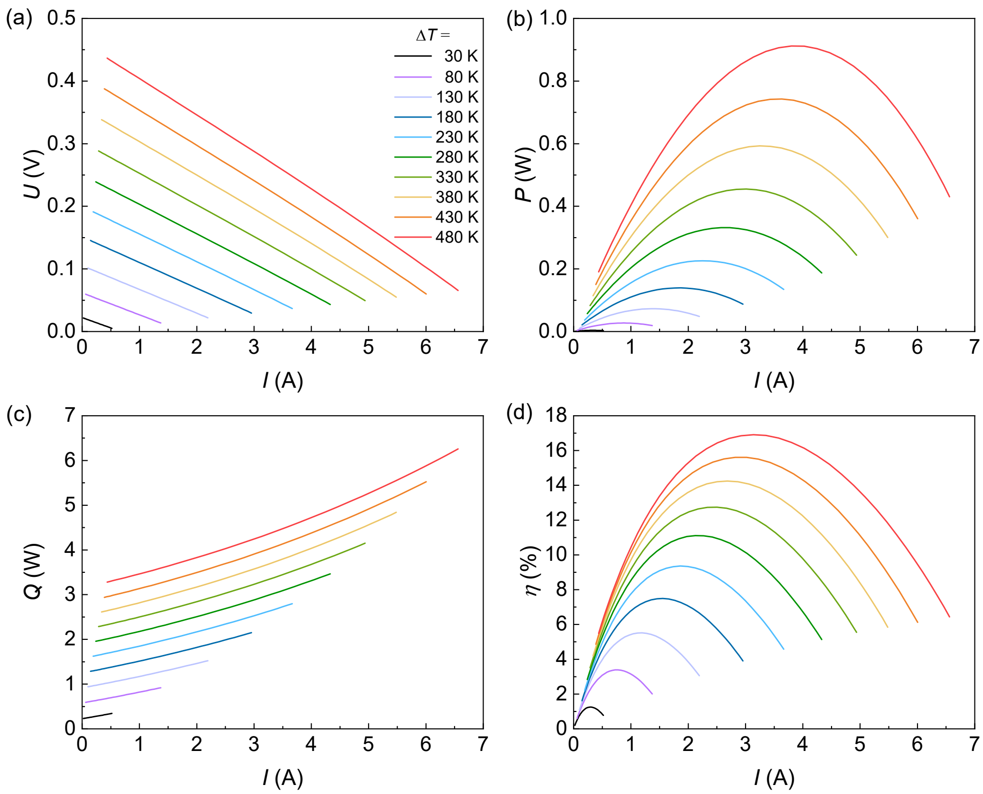

Fig. S14 Simulated properties of the ($Mg_{3.15}Co_{0.05}Sb_{1.24}Bi_{0.75}Se_{0.01}$/$(Pb_{0.15}Ge_{0.85}Te)_{0.8}(AgSbTe_2)_{0.2}$) module. Current-dependent (a) output voltage, (b) output power, (c) heat flow, and (d) efficiency for the module at different temperature differences.

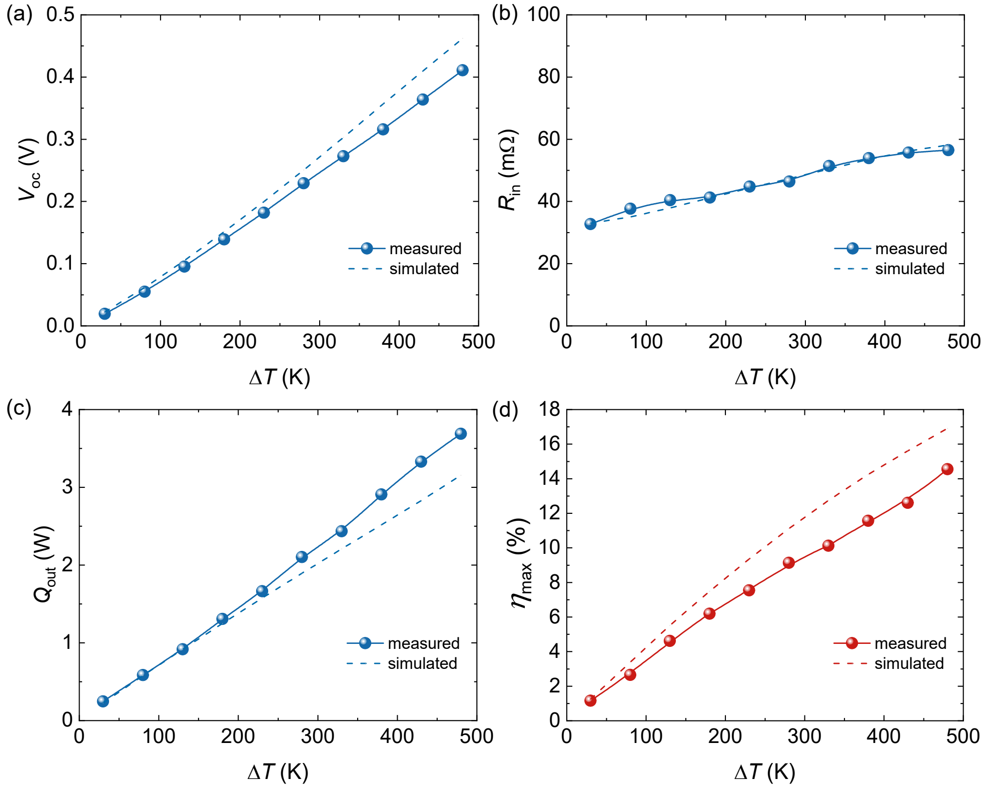

s

Fig. S15 Experimental and simulated current-dependent (a) open-circuit voltage (V_{oc}), (b) internal resistance (R_{in}) (c) maximum output heat flow, and (d) conversion efficiency at different temperature differences.

Reference

1. Z. M. Gibbs, H.-S. Kim, H. Wang and G. J. Snyder, *Appl. Phys. Lett.*, 2015, **106**, 022112.
2. M. T. Agne, K. Imasato, S. Anand, K. Lee, S. K. Bux, A. Zevalkink, A. J. E. Rettie, D. Y. Chung, M. G. Kanatzidis and G. J. Snyder, *Mater. Today Phys.*, 2018, **6**, 83-88.